Splitting CO_2 with a Ceria-Based Redox Cycle in a Solar-Driven Thermogravimetric Analyzer

M. Takacs
Dept. of Mechanical and Process Engineering, ETH Zurich, Zurich 8092, Switzerland

S. Ackermann
Dept. of Mechanical and Process Engineering, ETH Zurich, Zurich 8092, Switzerland

A. Bonk
Laboratory of Materials for Energy Conversion, EMPA, Dübendorf 8600, Switzerland

Institute for Geo- and Life Sciences, Crystallography, Albert-Ludwigs-Universität Freiburg, Freiburg 79085, Germany

M. Neises-von Puttkamer
Institute of Solar Research, German Aerospace Center, Linder Höhe, Köln 51147, Germany

Ph. Haueter
Dept. of Mechanical and Process Engineering, ETH Zurich, Zurich 8092, Switzerland

J. R. Scheffe
Dept. of Mechanical and Aerospace Engineering, University of Florida, Gainesville, FL 32611

U. F. Vogt
Laboratory of Materials for Energy Conversion, EMPA, Dübendorf 8600, Switzerland

Institute for Geo- and Life Sciences, Crystallography, Albert-Ludwigs-Universität Freiburg, Freiburg 79085, Germany

A. Steinfeld
Dept. of Mechanical and Process Engineering, ETH Zurich, Zurich 8092, Switzerland

Thermochemical splitting of CO_2 via a ceria-based redox cycle was performed in a solar-driven thermogravimetric analyzer. Overall reaction rates, including heat and mass transport, were determined under concentrated irradiation mimicking realistic operation of solar reactors. Reticulated porous ceramic (RPC) structures and fibers made of undoped and Zr^{4+}-doped CeO_2, were endothermally reduced under radiative fluxes of 1280 suns in the temperature range 1200–1950 K and subsequently re-oxidized with CO_2 at 950–1400 K. Rapid and uniform heating was observed for 8 ppi ceria RPC with mm-sized porosity due to its low optical thickness and volumetric radiative absorption, while ceria fibers with μm-sized porosity performed poorly due to its opacity to incident irradiation. The 10 ppi RPC exhibited higher fuel yield because of its higher sample density. Zr^{4+}-doped ceria showed increasing reduction extents with dopant concentration but decreasing specific CO yield due to unfavorable oxidation thermodynamics and slower kinetics. © 2016 The Authors AIChE Journal published by Wiley Periodicals, Inc. on behalf of American Institute of Chemical Engineers AIChE J, 63: 1263–1271, 2017
Keywords: solar fuels, doped ceria, thermochemical, kinetics, heat transfer

Introduction

Using concentrated solar energy, thermochemical redox cycles based on nonstoichiometric metal oxides are capable of splitting H_2O and CO_2 to produce H_2 and CO (syngas), the precursor for the synthesis of conventional transportation liquid fuels.[1] Due to its favorable oxidation thermodynamics, rapid reaction kinetics, and morphological stability over a wide range of temperatures, ceria (CeO_2) is currently considered the

benchmark redox material.[2–7] The two-step thermochemical cycle is then represented by:

Reduction at T_{red}:

$$\frac{1}{\delta_{red}-\delta_{ox}}CeO_{2-\delta_{ox}} \rightarrow \frac{1}{\delta_{red}-\delta_{ox}}CeO_{2-\delta_{red}} + \frac{1}{2}O_2 \quad (1)$$

Oxidation at T_{ox}:

$$\frac{1}{\delta_{red}-\delta_{ox}}CeO_{2-\delta_{red}} + H_2O \rightarrow \frac{1}{\delta_{red}-\delta_{ox}}CeO_{2-\delta_{ox}} + H_2 \quad (2a)$$

$$\frac{1}{\delta_{red}-\delta_{ox}}CeO_{2-\delta_{red}} + CO_2 \rightarrow \frac{1}{\delta_{red}-\delta_{ox}}CeO_{2-\delta_{ox}} + CO \quad (2b)$$
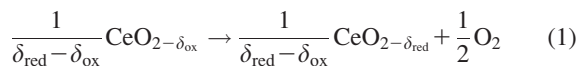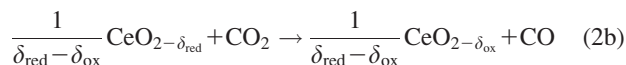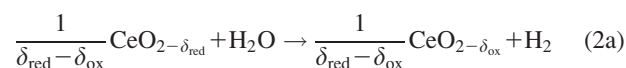
where δ_{ox} and δ_{red} are the oxygen nonstoichiometry before and after reduction, respectively. In the first step, Eq. 1, ceria is endothermally reduced in an atmosphere of low oxygen partial pressure p_{O2} at elevated temperatures, typically $T_{red} > 1573$ K, with process heat delivered by concentrated solar radiation. In the second step, Eq. 2, the reduced ceria is exothermally re-oxidized with H_2O and/or CO_2 to generate H_2 and/or CO at lower temperatures, typically $T_{ox} < 1573$ K. δ_{red} and δ_{ox} at equilibrium strongly depend on T_{red}, T_{ox}, and p_{O2}.[2,8–10] The difference $\delta_{red} - \delta_{ox}$ determines the maximum molar amount of fuel capable of being produced per cycle and per mole of ceria. Various porous ceria structures have been investigated such as 3D ordered macroporous structures,[11] electrospun fibers,[12] monoliths,[13] felts,[14] and reticulated porous ceramics (RPC).[14] Although structures with submicron-sized pores exhibited relatively fast oxidation rates, they lacked morphological stability as sintering occurred at elevated temperatures.[11] Furthermore, optically thick structures inhibited penetration of concentrated solar irradiation, resulting in non-uniform heating and, consequently, non-uniform temperature distribution.[15] In contrast, the foam-type RPC structures offered enhanced heat and mass transport properties for high-temperature processing.[16] They have been developed with interconnected single-scale porosity (SS-RPC)[15] as well as with interconnected dual-scale porosity (DS-RPC).[17,18] In the latter, the larger mm-sized pores enabled efficient volumetric radiative absorption during reduction (Eq. 1) due to appropriate optical thickness, while the smaller μm-sized pores within the struts enabled fast reaction rates during oxidation with CO_2 and H_2O (Eq. 2) due to an increased specific surface area.[17] RPCs with 76% overall porosity and 18% strut porosity, obtained by the addition of 30 vol % carbon pore forming agent into the ceramic slurry,[17,19] offered a trade-off between large specific surface area (0.066 m^2 g^{-1}) for fast oxidation kinetics and large mass loading per unit volume for high fuel yield, while being morphologically stable over more than 200 redox cycles at $T_{red} = 1773$ K and $T_{ox} = 1023$ K.[18] The specific fuel yield per cycle, given by $\delta_{red} - \delta_{ox}$, can be increased by alternative redox materials with a higher oxygen exchange capacity compared to ceria,[20] for example by the introduction of 4+ valence dopants such as Zr^{4+} [2,21–26] or Hf^{4+}.[21,27] However, their oxidation is thermodynamically less favorable compared to undoped ceria, which leads to substantially larger temperature swings between reduction and oxidation steps, ultimately resulting in slower oxidation rates[19,21] and lower theoretical solar energy conversion efficiencies compared with ceria under most conditions unless heat is recovered between the temperature-swing operation.[2,3]

In this work, we investigate the overall rates of redox reactions, including heat and mass transport phenomena, using a solar-driven thermogravimetric analyzer (solar-TG), in which the RPC structures are directly exposed to high-flux irradiation while their mass change is continuously monitored. With this arrangement, the overall rates can be determined under similar radiative heat transfer characteristics typical of high-temperature solar reactors operated in concentrating solar systems such as solar towers and dishes, thus mimicking realistic operating conditions.[28,29] Measurements using a standard thermogravimetric analyzer cannot supply the same data because samples are not irradiated and heat/mass transfer effects are eliminated to ensure the data is about the intrinsic reaction kinetics only. Measurements using a solar reactor are unpractical because of the large volume of the sample required to fill the cavity and because the weight change of the sample cannot be monitored. Supplementing previous studies with RPC structures performed in solar reactors[15,18] and standard thermogravimetric analyzers,[17] this work further investigates the influence of the porous structure and Zr-dopant concentration on the overall rates of both reduction/oxidation reactions, as well as on the reduction extent and specific fuel yield, with samples subjected to high-flux conditions relevant to the operation of solar reactors. We analyze the O_2 and CO evolutions during reduction and oxidation, respectively, of SS-RPC, DS-RPC, and fibers made of undoped ceria. Additionally, DS-RPC samples made of ceria doped with 10 and 20 mol % Zr^{4+} are compared with those made of undoped ceria. The sample morphology before and after redox cycling is investigated by scanning electron microscopy (SEM); the phase composition by powder x-ray diffraction (XRD). As it will be shown in the analysis that follows, the results help elucidate the rate limiting mechanisms for each step of the redox cycle and guide the design of materials and structures for improving the cycle performance.

Experimental

Sample preparation and characterization

DS- and SS-RPC samples of composition $Zr_xCe_{1-x}O_2$ ($x = 0$, 0.1, and 0.2) were produced by the replication method.[30] CeO_2 powder (Sigma Aldrich, 99.9% purity, particle size < 5 μm), stoichiometric amounts of ZrO_2 (Tosoh, TZ-0, 99.95% purity, surface area 14.5 m^2 g^{-1}), and 30 vol % spherical carbon pore-forming agent particles (HTW Hochtemperatur-Werkstoffe GmbH, Sigradur K, particle size 0.4–12 μm, for DS-RPC samples) were mixed with water in a 5:1 mass ratio. 0.84 wt % organic deflocculating agent (Zschimmer & Schwarz, Dolapix CE64), 20 wt % polyvinyl alcohol binder (PVA, Zschimmer & Schwarz, Optapix RA 4G) and antifoaming agent (Zschimmer & Schwarz, Contraspum KWE) were added and processed according to a previously reported recipe.[17,31] Organic polyurethane sponges (Foam Partner, Fritz Nauer AG) with 8, 10, and 35 pores per inch (ppi) were then immersed into the slurry, dried in air, and finally sintered for 5 h at 1873 K. The solid-to-water ratio was decreased linearly for the ZrO_2 containing RPCs from 5:1 for $x = 0$ to 4.8:1 for $x = 0.2$ due to the increasing viscosity with ZrO_2 content. Figure 1 shows photographs of the ceria RPC structures with 8, 10, and 35 ppi in the mm-scale, and 18% porosity within the struts in the μm-scale. The approximate dimensions of all the RPC samples after sintering were 30 mm diameter and 18 mm thickness. Also shown is a photo of the commercially available ceria fiber sample (Zircar Zirconia, 88% porosity, mean fiber dimensions: 7 μm-diameter, 100 μm-length). Large (mm-range) and small scale (μm-range)
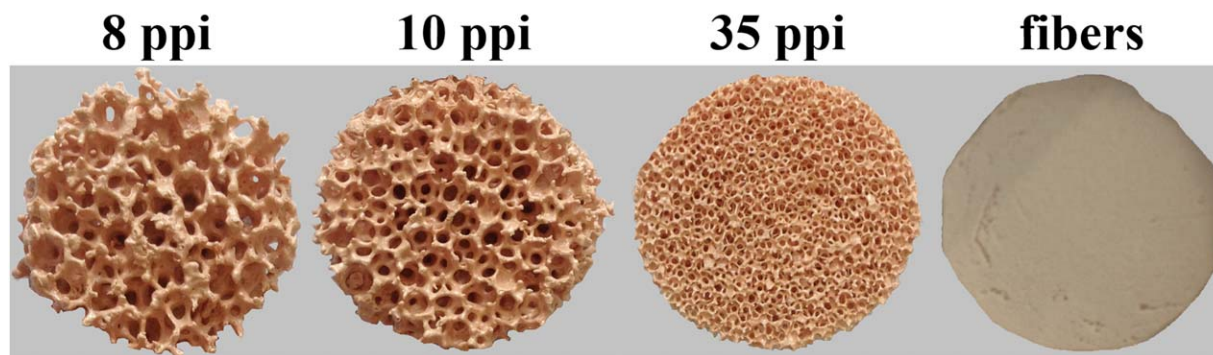
Figure 1. Photographs of ceria DS-RPC structures with 8, 10, and 35 ppi in the mm-scale and 18% porosity within the struts in the μm-scale. Also shown is the ceria fiber sample with 88% porosity in the μm-scale.

[Color figure can be viewed at wileyonlinelibrary.com]

porosity, as well as mass and density of all the samples prepared for testing in the solar-TG are summarized in Table 1. The 10 ppi ceria SS-RPC is the sample with the highest density (2.12 g cm^{-3}) because of its non-porous struts. Among the DS-RPC with porous struts, the 10 ppi sample has the highest density because of its smallest mm-sized pores and largest strut thickness. The strut thickness depended on the viscosity of the slurry and on the number of coating layers. The 8 and 10 ppi RPC samples were coated twice, while the 35 ppi RPC sample was coated only once because of the small pores. The different values of density of the Zr-doped RPC samples were also due to the strut thickness obtained during manufacturing with a different slurry when adding Zr. XRD was performed in parallel-beam geometry using Cu Kα radiation (Philips, PANalytical/X'Pert MPD/DY636, $\lambda = 1.5418$ Å, $2\Theta = 20–95°$, $1.0° \text{ min}^{-1}$ scan rate). XRD patterns are shown in the electronic supplementary information (ESI)*. SEM was performed on an ESEM XL30 Microscope (FEI, 10 kV accelerating voltage). SS-RPC structures made of Al_2O_3 with same dimensions were identically fabricated for the thermogravimetric buoyancy correction.

Experimental set-up

The solar-driven thermogravimetric analyzer is schematically shown in Figure 2. The setup consists of an Al_2O_3 rod of 12 mm outer diameter, 340 mm length, and 2 mm wall thickness, suspended on top of a balance (WMS404C, Mettler Toledo, 0.1 mg accuracy) and enclosed in a stainless steel housing. The RPC sample is placed on top of a ZrO_2 porous platform (30 ppi, Spohr GmbH, 24 mm height, 30 mm diameter) positioned on the Al_2O_3 rod. The RPC sample is covered with a transparent quartz dome (Schmizo, 70 mm outer diameter, 150 mm height, 2.5 mm wall thickness) that is sealed to the metallic housing with a refrigerated O-ring flange. The

temperature of the bottom of the RPC is measured by a wireless type-S thermocouple (Omega, MWTC-A-S-868 and MWTC-REC6) to eliminate disturbance of the balance. Temperatures are also measured along the centerline of the RPC at $z = 2$, 7, and 12 mm below the top surface of the RPC in separate experiments where the balance is disconnected (accuracy of thermocouple placement was ± 2 mm). A refrigerated brass jacket (63 mm outer diameter, 48 mm inner diameter, and 76 mm length) lined with an Al_2O_3 fiber ring (4 mm thickness, 64 mm height) is placed around the RPC on the inner side of the quartz dome. A tangential gas inlet through the top of the quartz dome enables the injection of Ar sweep gas during the reduction step and of CO_2 during the oxidation step. The product gas exits through an outlet port located 100 mm below the RPC and is cooled by a gas cooler (AGT Thermotechnik GmbH, MAK 10). Mass flow rates are electronically controlled (Bronkhorst HIGH-TECH B.V., EL-FLOW). The product gas composition is analyzed by infrared (IR) sensors for CO and CO_2 and an electrochemical sensor for O_2 (Siemens Ultramat 23), and verified by gas chromatography (Varian, CP-4900 Micro GC).

Experimentation was performed at the high-flux solar simulator (HFSS) of ETH Zurich. An array of seven Xe-arcs, close-coupled to truncated ellipsoidal reflectors, provided an external source of intense thermal radiation, mostly in the visible and IR spectra, that closely approximates the heat transfer characteristics of highly concentrating solar systems.[32] The concentrated radiation was redirected by a 45°-tilted mirror and focused on the top surface of the RPC. The radiative flux distribution on the plane of that surface was determined prior to the solar-TG runs by using a CCD camera (BASLER, A 1021) focused on a water-cooled, Al_2O_3 plasma-coated Lambertian (diffusely reflecting) target. The total solar radiative power input on the sample surface was calculated by flux

Table 1. Large (mm-Range) and Small Scale (μm-Range) Porosity, as Well as Mass and Density of All the Samples Prepared for Testing in the Solar-TG

| Sample	Large Scale Porosity (mm-Range)	Small Scale Porosity (μm-Range)	Material	Mass (g)	Density (g cm^{-3})
8 ppi ceria DS-RPC	8 ppi	18% Ref. 17	CeO$_2$	16.42	1.26
10 ppi ceria DS-RPC	10 ppi	18% Ref. 17	CeO$_2$	18.41	1.41
35 ppi ceria DS-RPC	35 ppi	18% Ref. 17	CeO$_2$	11.63	0.89
10 ppi ceria SS-RPC	10 ppi	none	CeO$_2$	27.71	2.12
ceria fiber sample	none	88%	CeO$_2$	9.65	0.86
10 ppi CZO_10 DS-RPC	10 ppi	18% Ref. 17	10 mol % Zr doped CeO$_2$	16.39	1.26
10 ppi CZO_20 DS-RPC	10 ppi	18% Ref. 17	20 mol % Zr doped CeO$_2$	20.45	1.57
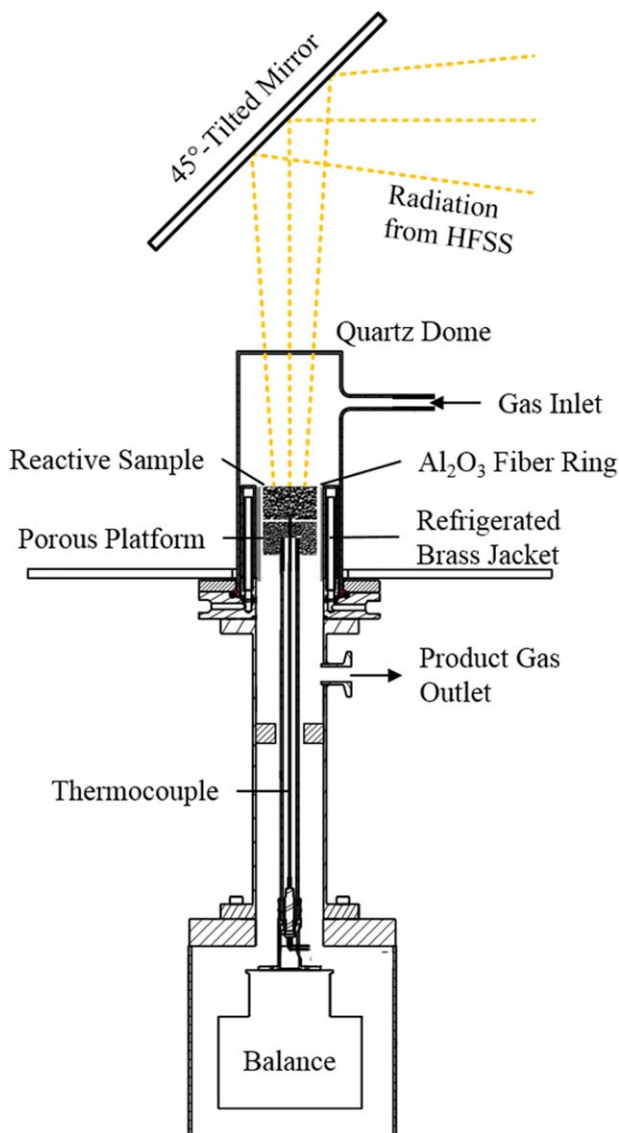
Figure 2. Schematic of the solar-driven thermogravimetric analyzer. Concentrated radiation delivered by the High-Flux Solar Simulator (HFSS) is redirected by a 45°-tilted mirror, enters the setup through a transparent quartz dome, and is incident on the RPC sample whose weight change and gas evolution are temporally monitored.

[Color figure can be viewed at wileyonlinelibrary.com]

integration and verified by water calorimetry. During a typical redox cycle, the system was first purged with Ar (Messer, Argon 4.6) until $p_{O2} < 0.2$ mbar was reached in the outlet gas. At time $t = 0$ min, the HFSS was switched on and the RPC sample was exposed to a mean radiative flux of 128 W cm^{-2} (1280 suns) under an Ar gas flow rate of 0.5 L min^{-1}. After 10 min of reduction, the radiative flux was decreased to 44 W cm^{-2} (440 suns) and the samples cooled for 30 s. Afterwards, the gas flow was switched to 0.5 L min^{-1} CO$_2$ (Messer, Carbon Dioxide 4.8). After 9 min of oxidation with CO$_2$, the next cycle was initiated by switching the gas flow back to Ar and increasing the solar flux. Note that although the re-oxidation step is exothermic (Eq. 2ab), the HFSS was not completely switched off to counter-balance the heat losses and

maintain a constant T_{ox}. Three consecutive redox cycles were performed with each sample. In the first cycle the sample was heated from ambient temperature to T_{red} whereas in the second and third cycle it was heated from T_{ox}.

Buoyancy effects were accounted by subtracting the weight change obtained with blank runs using unreactive samples made of Al$_2$O$_3$ and having equivalent porous structures, namely: 8, 10, and 35 ppi RPC and fibers. Although it was not possible to apply the buoyancy corrections at the exact same temperature for each reactive sample, the maximum relative temperature difference was less than 6.4%, 8.0%, 4.0%, and 3.8% for the 8, 10, and 35 ppi RPC and the fiber sample, respectively. This, in turn, led to an uncertainty in the weight change measurement of less than 7% of the absolute measured weight change for all samples at all times. Since the solar radiative input power and the solar radiative fluxes incident on the RPC are main design parameters of the solar reactor,[13,18] O$_2$ and CO evolutions are compared for samples exposed to the same incident radiative fluxes, i.e., 1280 suns during reduction and 440 suns during oxidation for all experimental runs. This way, the effect of the porous structure (porosity and pore size) on the overall kinetics can be assessed, including heat and mass transfer limitations during both redox steps, and the results can be directly applied to guide the design of these structures for solar reactors.

Results and Discussion

Figure 3 shows a representative solar-TG run with the 10 ppi ceria DS-RPC (19 mm height, 18.4 g mass): Figure 3a shows temperature as a function of time at $z = 2$, 7, and 12 mm below the top surface of the RPC; Figure 3b shows the corresponding weight change vs. time, and Figure 3c shows the corresponding specific gas evolution rates vs. time The RPC was heated at an average rate of 100 K s^{-1} for the first 10 s at $z = 2$ mm, faster than at the center and bottom because radiation was efficiently absorbed in the first layers while heat was internally transferred to the bottom by combined conduction, convection, and re-radiation. Approximate steady-state temperatures of 1900, 1670, and 1590 K were obtained at $z = 2$, 7, and 12 mm, respectively. During reduction under Ar, the RPC underwent a weight decrease by 0.35% accompanied by O$_2$ evolution within the allotted 10 min. During oxidation with CO$_2$ at $T_{ox} = 1400$, 1200, and 1110 K at $z = 2$, 7, and 12 mm, respectively, the weight increased and CO evolved, but complete oxidation was not reached within the allotted 9 min. For the 1st cycle, the specific O$_2$ and CO amounts evolved, as obtained by integration of the curves of Figure 3c, were 2.54 and 4.38 mL g^{-1}, respectively, yielding a CO:O$_2$ molar ratio of 1.72 due to the incomplete oxidation. During the subsequent cycles, CO:O$_2$ molar ratio was 2 ± 0.05, confirming closed mass balance and full selectivity of CO$_2$ to CO. The total amount of O$_2$ released, as measured by the gas analysis, agreed well with the weight change measurement within 7%. Temporal variations of temperatures, weight, and gas evolution were reproducible during the three consecutive redox cycles.

Optical thickness

The influence of the sample's optical thickness on the heating rate and specific fuel yield was investigated by testing ceria DS-RPCs with 8, 10, and 35 ppi as well as the ceria fiber sample (cf. Figure 1) of similar dimensions (RPCs: ~18 mm thickness, ~30 mm diameter; fiber sample: ~14 mm
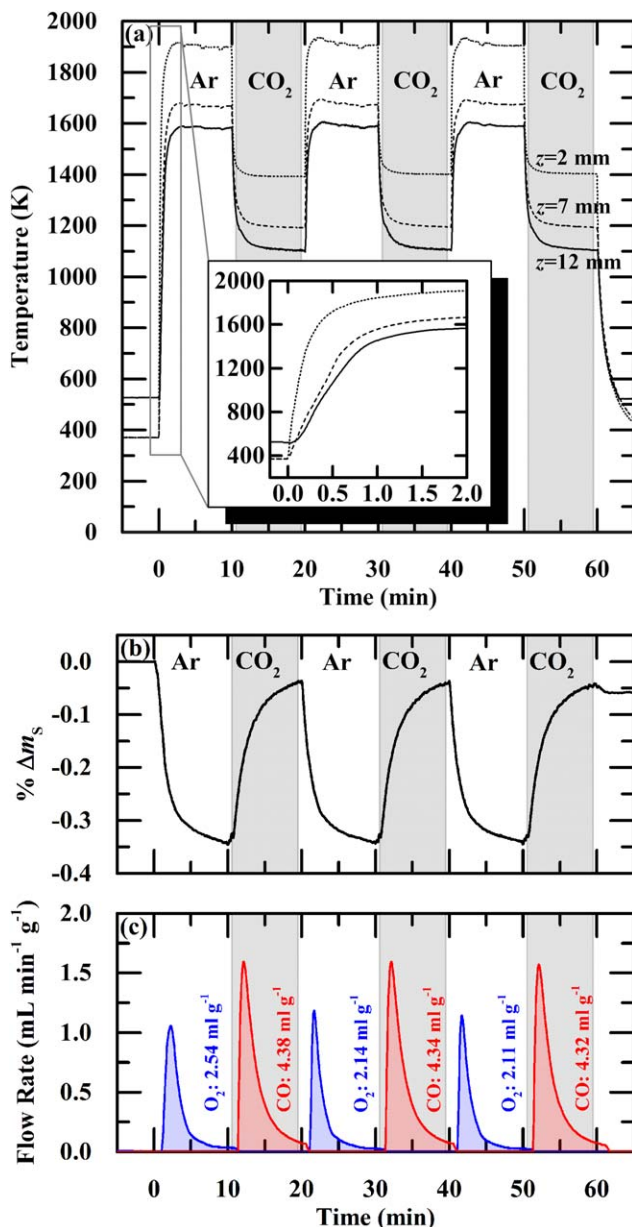
Figure 3. Solar-TG measurements for the 10 ppi ceria DS-RPC.

(a) Temperature as a function of time at $z = 2$ mm (dotted lines), 7 mm (dashed lines), and 12 mm (solid lines) below the top surface during 3 consecutive redox cycles.

(b) Corresponding %-mass change.

(c) Corresponding mass specific O_2 and CO evolution rates as well as the integrated mass specific O_2 and CO evolved. [Color figure can be viewed at wileyonlinelibrary.com]

ppi RPC and 11 K s^{-1} for the 35 ppi RPC. The steady-state temperatures achieved at the bottom of the RPC samples increased with the large-scale pore size, from around 1540 K for the 35 ppi to 1625 K for the 8 ppi, as a result of the deeper penetration and volumetric absorption of concentrated radiation. In contrast, the fiber sample achieved the lowest steady-state temperature of around 1330 K at the bottom because of opacity to incident radiation, leading to inefficient heating. Typical mean values of the effective extinction coefficient were 280 m^{-1} for the RPC and 40,000 m^{-1} for the fiber, indicating two orders of magnitude higher optical thickness for the latter.[15] The highest specific weight loss was observed for the 10 ppi RPC, even though the highest temperature was measured for the 8 ppi RPC, because of its high sample density (*cf.* Table 1) in combination with its relatively large pores. The time required for releasing 2.5 mg cm^{-3} of O_2 was approximately 1.3, 1.9, and 3.1 min for the 10, 8, and 35 ppi RPC, respectively. For a constant radiative power input of 128 W cm^{-2}, this implies that 140% more energy was needed to
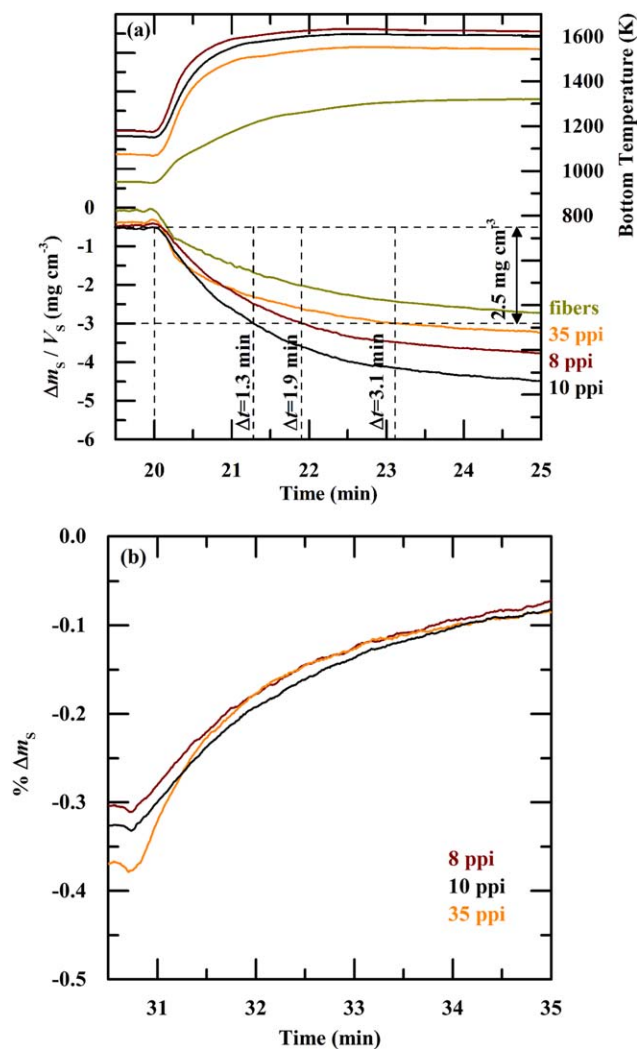

Figure 4. Solar-TG measurements of the 8, 10, and 35 ppi ceria DS-RPC and the ceria fiber sample.

(a) Bottom temperature and specific weight change as a function of time during reduction.

(b) Percent weight change during oxidation with CO_2 at around 1150 K bottom temperature. [Color figure can be viewed at wileyonlinelibrary.com]

thickness, ~32 mm diameter) but different mass as listed in Table 1. The solar-TG measurements of these samples are shown in Figure 4. Figure 4a shows the bottom temperature and the specific weight loss as a function of time during reduction and Figure 4b shows percent weight change of the 8, 10, and 35 ppi ceria DS-RPC during oxidation with CO_2 at around 1150 K bottom temperature. The 8 ppi ceria RPC underwent the fastest heating, followed by the 10 ppi, the 35 ppi and the fiber sample, as expected. The average heating rate from 1200 to 1400 K was 16 K s^{-1} for the 8 ppi RPC, 12 K s^{-1} for the 10
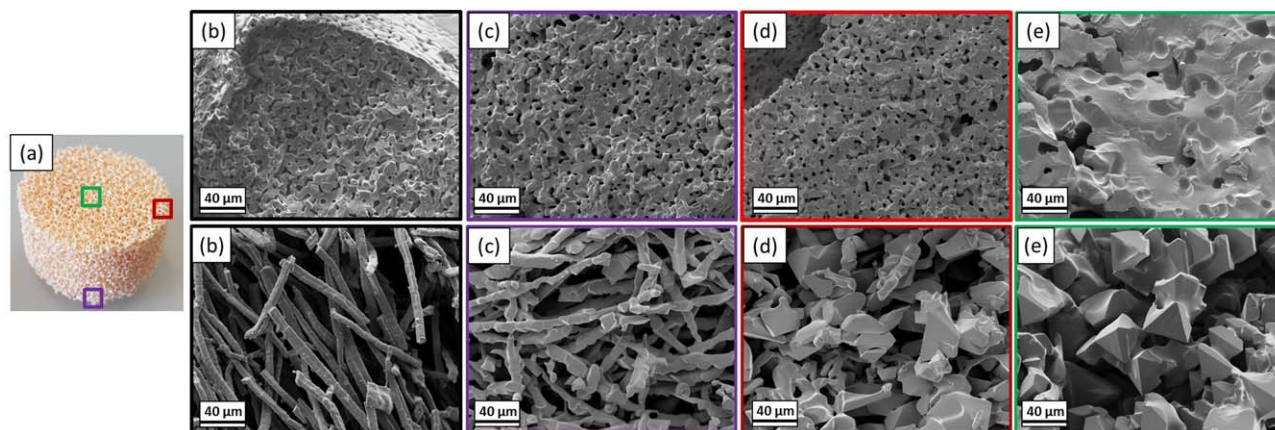
Figure 5. SEM images of the 10 ppi ceria DS-RPC (1st row) and of the ceria fiber sample (second row).

(a) Locations where the SEM images were taken.

(b) Before redox cycling.

(c) After redox cycling at the edge of the bottom surface.

(d) After redox cycling at the edge of the top surface.

(e) After redox cycling at the center of the irradiated top surface. [Color figure can be viewed at wileyonlinelibrary.com]

reduce the 35 ppi RPC compared with the 10 ppi RPC. The oxidation rates with CO_2 were very similar for all the RPC samples tested, as shown in Figure 4b, because of their similar specific surface area (0.066 m^2 g^{-1})[17] that is mainly determined by the μm-sized porosity of the struts. The 10 ppi DS-RPC produced the largest amounts of CO, as obtained by multiplying the curves in Figure 4b with the corresponding densities. Thus, because of the very similar oxidation rates, the redox performance of the various DS-RPC structures can be assessed by simply comparing their volume-specific O_2 release during reduction (*cf*. Figure 4).

Figure 5 shows the SEM images of strut brake planes of the 10 ppi ceria DS-RPC (1st row of images) and of the ceria fiber sample (second row of images): (a) locations where the SEM images were taken; (b) before redox cycling; (c) after redox cycling at the edge of the bottom surface; (d) after redox cycling at the edge of the top surface; and (e) after redox cycling at the center of the irradiated top surface. For the RPC, morphological changes were predominantly observed at the center of the irradiated top surface directly exposed to 1660 suns (*cf*. Figure 2 in ESI), resulting in temperatures exceeding 1900 K that lead to grain growth and partial sintering of the μm-sized pores, as shown in Figure 5e. Nevertheless, no significant decrease in redox performance was observed during three consecutive redox cycles (*cf*. Figure 3 for the 10 ppi ceria DS-RPC). For the fiber sample, grain growth was observed over the entire sample surface, becoming more pronounced toward the center of the irradiated top surface where the fiber structure was completely destroyed.

Single- vs. dual-scale porosity

The influence of the strut porosity on the specific fuel yield was investigated by comparing the redox performance of the 10 ppi SS-RPC (no porous struts) and the 10 ppi DS-RPC (porous struts). Figure 6 shows the temporal variation during the second redox cycle of: (a) the volume-specific O_2 and CO evolution rates along with the bottom temperature, (b) the cumulative mass-specific CO yield; and (c) the cumulative volume-specific CO yield. Integration of the O_2 and CO curves

of Figure 6a reveals that the SS-RPC released more O_2 and consequently produced more CO compared to the DS-RPC, mainly because of its higher density: 2.12 g cm^{-3} for the SS-RPC vs. 1.41 g cm^{-3} for the DS-RPC. However, due to the larger specific surface area of the RPC with μm-size strut porosity,[17] the DS-RPC exhibited faster oxidation rates, as shown by the mass specific CO production in Figure 6b. These results are in full agreement with the experiments carried out with a solar reactor, where time duration of the oxidation step was cut from 20 min for the SS-RPC to 8 min for the DS-RPC.[18] Conversely, Figure 6c confirms that, in terms of volume-specific fuel yields, the SS-RPC is superior to the DS-RPC because of the higher density.

Undoped ceria vs. Zr⁴⁺-doped ceria

Figure 7a shows the percent weight change as a function of time during three consecutive redox cycles of the 10 ppi DS-RPCs made of undoped ceria, 10 mol % Zr^{4+}-CeO_2 (CZO_10), and 20 mol % Zr^{4+}- CeO_2 (CZO_20), as well as their corresponding bottom temperature. The corresponding mass-specific O_2 and CO evolutions are shown in (b) and (c), respectively. The highest mass loss was measured for CZO_20, followed by CZO_10 and undoped ceria, leading to a mass-specific O_2 release of 4.2 mL g^{-1} for CZO_20, followed by 3.3 mL g^{-1} for CZO_10 and 2.6 mL g^{-1} for undoped ceria. This trend is in agreement with previous studies.[2,21–25] During the subsequent oxidation with CO_2, undoped ceria exhibited faster reaction rates and reached 80% oxidation extent to yield 4.4 mL g^{-1} CO within the allotted oxidation time of 9 min. Conversely, the oxidation of CZO_10 and CZO_20 was much slower and reached 50 and 25% oxidation extents, respectively, within 9 min to yield 2.8 and 1.5 mL g^{-1}, respectively, consistent with previous measurements.[19,21] Due to the incomplete oxidation, the O_2 release in the subsequent reduction steps decreased with higher Zr^{4+}-dopant concentration. To check whether oxidation rates were restricted by thermodynamic limitations, the maximum oxidation extents (equilibrium δ) at $t = 11.5$ min were determined by using thermodynamic data for Zr^{4+}-doped ceria[25] and
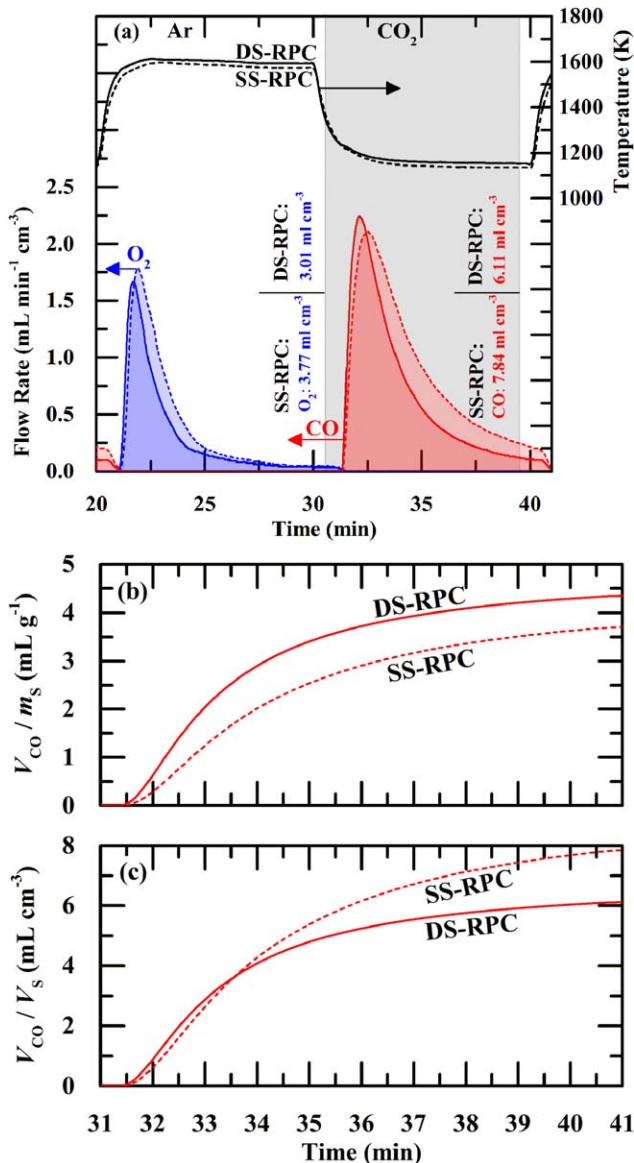
Figure 6. (a) Volume-specific flow rate of O_2 and CO as well as the bottom temperature of the RPC with single-scale porosity (SS-RPC) (dashed lines) and of the RPC with dual-scale porosity (DS-RPC) (solid lines) during the second redox cycle. Additionally, integrated mass specific O_2 release and CO yield are shown in (a). (b) Mass-specific and (c) volume-specific CO yield of both RPCs during the second oxidation.

[Color figure can be viewed at wileyonlinelibrary.com]

undoped ceria.[8] CO partial pressures were determined from the temporal weight gain of the samples in combination with the CO_2 inlet flow rate; it was assumed that CO and CO_2 were perfectly mixed. With the knowledge of p_{CO} and p_{CO_2} the corresponding p_{O_2} was calculated according to:

$$p_{O_2} = \left(K_f^{-1} \frac{p_{CO_2}}{p_{CO}} \right)^2 \tag{3}$$

where K_f is the equilibrium constant for the formation of CO_2 obtained from NIST-JANAF thermochemical tables. Comparing

the calculated thermodynamic weight losses to the measured ones reveals that the measured oxidation extents have not yet reached the thermodynamic limit. When assuming a constant RPC oxidation temperature of 1230 K, the measured weight change is 15, 40, and 300% lower than the thermodynamic limit for CZO_20, CZO_10, and undoped ceria, respectively. This is because the oxidation step was interrupted prior to its completion (see Figure 7a), as the reaction rate slowed down due presumably to high local CO concentrations, i.e., mass transfer limitations. Note, however, that the thermodynamic oxidation limit is closest to $\Delta m_S = 0$ for ceria, followed by CZO_10 and CZO_20 (solid lines in Figure 3 of ESI), which means that undoped ceria has the most favorable oxidation
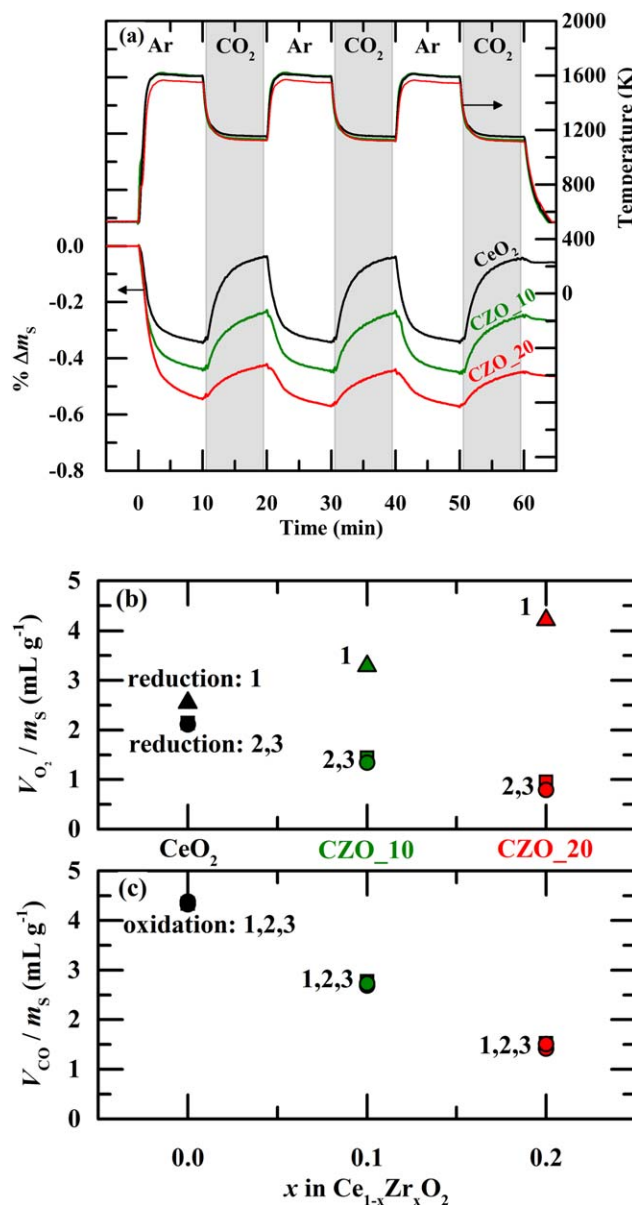

Figure 7. (a) Percent mass change and bottom temperature of the CeO_2, CZO_10 and CZO_20 DS-RPC sample with 10 ppi during the three redox cycles. Mass specific O_2 release (b) and CO productivity (c) during reduction steps 1, 2, and 3 vs. Zr^{4+}-dopant concentration x.

[Color figure can be viewed at wileyonlinelibrary.com]

thermodynamics.[8,25] A graphical representation of the thermo-dynamic limitation is shown in Figure 3 in ESI. We can conclude that at least under these assumptions none of the samples are in thermodynamic equilibriums with their surroundings and the rates are limited by chemical kinetics. But note that the temperature distribution of the RPC was not uniform (*cf.* Figure 3) and that the temporal p_{CO} inside the RPC is unknown; thus, an overall precise differentiation between thermodynamic and kinetic limitation is not possible.

Summary and Conclusions

RPC structures with SS-RPC and DS-RPC made of undoped, 10 and 20 mol % Zr^{4+}-doped ceria, as well as commercially available ceria fibers, were investigated for their redox performance to thermochemically split CO_2 using a solar-driven thermogravimetric analyzer under radiative heat fluxes characteristic of highly concentrating solar systems. The RPC with the largest mm-sized pores (8 ppi) featured efficient heat transfer because of its low optical thickness as indicated by the relatively higher heating rate and higher measured bottom temperature. In contrast, the highest volume-specific O_2 release and CO yield was obtained with the 10 ppi RPC because of its higher sample density. SEM images revealed grain growth and partial sintering of the strut's μm-scale pores at the top surface of the RPC that was directly exposed to a radiative flux of 1660 suns. The DS-RPC with mm-sized porosity containing struts with additional μm-sized porosity exhibited faster oxidation rates than those for the SS-RPC with dense struts without porosity because of the higher specific surface area, but yielded less CO per unit volume because of the lower sample density. Although Zr^{4+}-doped ceria showed increasing reduction extents with increasing dopant concentration, it could not be oxidized to a large extent due to unfavorable thermodynamics and slower kinetic rates, and hence yielded less CO compared with undoped ceria under the conditions investigated. The ceria fiber sample with only μm-sized porosity performed poorly in all aspects compared to RPC due mainly to its opacity to incident irradiation. In conclusion, for a limited RPC volume, the 10 ppi ceria DS-RPC offers the best trade-off in terms of fast heating rates, temperature uniformity, fast reaction rates, and high specific fuel yields.

Notation

Symbols

K_f = equilibrium constant of the CO_2 formation reaction
m_S = mass of reactive sample, g
Δm_S = relative mass change of reactive sample
p_g = partial pressure of gas g, bar
T = temperature, K
t = time, min
V_g = volume of gas g, mL
V_S = volume of reactive sample, cm^{-3}
x = Zr4+-dopant concentration
z = distance below sample top surface, mm
δ_{ox} = degree of oxygen nonstoichiometry after oxidation
δ_{red} = degree of oxygen nonstoichiometry after reduction

Abbreviations

CZO_10 = 10 mol % Zr^{4+}-doped ceria
CZO_20 = 20 mol % Zr^{4+}-doped ceria
DS-RPC = reticulated porous ceramic with dual-scale porosity
HFSS = high-flux solar simulator
IR = infrared
L = standard liters (at 273.15 K and 1 atm)
ppi = pores per inch
RPC = reticulated porous ceramic
SEM = scanning electron microscopy

SS-RPC = reticulated porous ceramic with single-scale porosity
TG = thermogravimetric analyzer
XRD = x-ray diffraction

Literature Cited

1. Romero M, Steinfeld A. Concentrating solar thermal power and thermochemical fuels. *Energy Environ Sci.* 2012;5(11):9234–9245.
2. Takacs M, Scheffe JR, Steinfeld A. Oxygen nonstoichiometry and thermodynamic characterization of Zr doped ceria in the 1573-1773 K temperature range. *Phys Chem Chem Phys.* 2015;17(12):7813–7822.
3. Scheffe JR, Steinfeld A. Thermodynamic analysis of cerium-based oxides for solar thermochemical fuel production. *Energy Fuel.* 2012;26(3):1928–1936.
4. Scheffe JR, Weibel D, Steinfeld A. Lanthanum–strontium–manganese perovskites as redox materials for solar thermochemical splitting of H_2O and CO_2. *Energy Fuel.* 2013;27(8):4250–4257.
5. Chueh WC, Haile SM. A thermochemical study of ceria: exploiting an old material for new modes of energy conversion and CO_2 mitigation. *Philos Trans A Math Phys Eng Sci.* 2010;368(1923):3269–3294.
6. Knoblauch N, Dorrer L, Fielitz P, Schmucker M, Borchardt G. Surface controlled reduction kinetics of nominally undoped polycrystalline CeO_2. *Phys Chem Chem Phys.* 2015;17(8):5849–5860.
7. Bulfin B, Call F, Lange M, Lange M, Lübben O, Sattler C, Pitz-Paal R, Shvets IV. Thermodynamics of CeO_2 thermochemical fuel production. *Energy Fuels.* 2015;29(2):1001–1009.
8. Panlener RJ, Blumenthal RN, Garnier JE. A thermodynamic study of nonstoichiometric cerium dioxide. *J Phys Chem Solids.* 1975;36(11):1213–1222.
9. Bevan DJM, Kordis J. Mixed oxides of the type MO_2 (fluorite)-M_2O_3-I Oxygen dissociation pressures and phase relationships in the system CeO_2-Ce_2O_3 at high temperatures. *J Inorganic Nuclear Chem.* 1964;26(9):1509–1523.
10. Bulfin B, Lowe AJ, Keogh KA, Murphy BE, Lübben O, Krasnikov SA, Shvets IV. Analytical model of CeO_2 oxidation and reduction. *J Phys Chem C.* 2013;117(46):24129–24137.
11. Venstrom LJ, Petkovich N, Rudisill S, Stein A, Davidson JH. The effects of morphology on the oxidation of ceria by water and carbon dioxide. *J Solar Energy Eng.* 2011;134(1):011005-011005–8.
12. Gibbons WT, Venstrom LJ, De Smith RM, Davidson JH, Jackson GS. Ceria-based electrospun fibers for renewable fuel production via two-step thermal redox cycles for carbon dioxide splitting. *Phys Chem Chem Phys.* 2014;16(27):14271–14280.
13. Chueh WC, Falter C, Abbott M, Scipio D, Furler Ph, Haile SM, Steinfeld A. High-flux solar-driven thermochemical dissociation of CO_2 and H_2O using nonstoichiometric ceria. *Science.* 2010;330(6012):1797–1801.
14. Furler P, Scheffe JR, Steinfeld A. Syngas production by simultaneous splitting of H_2O and CO_2 via ceria redox reactions in a high-temperature solar reactor. *Energy Environ Sci.* 2012;5(3):6098–6103.
15. Furler P, Scheffe J, Gorbar M, Moes L, Vogt U, Steinfeld A. Solar thermochemical CO_2 splitting utilizing a reticulated porous ceria redox system. *Energy Fuel.* 2012;26(11):7051–7059.
16. Haussener S, Coray P, Lipiński W, Wyss P, Steinfeld A. Tomography-based heat and mass transfer characterization of reticulate porous ceramics for high-temperature processing. *J Heat Transfer.* 2009;132(2):023305023305.
17. Furler P, Scheffe J, Marxer D, Gorbar M, Bonk A, Vogt U, Steinfeld A. Thermochemical CO_2 splitting via redox cycling of ceria reticulated foam structures with dual-scale porosities. *Phys Chem Chem Phys.* 2014;16(22):10503–10511.
18. Marxer D, Furler P, Scheffe J, Geerlings H, Falter C, Batteiger V, Sizmann A, Steinfeld A. Demonstration of the entire production chain to renewable kerosene via solar thermochemical splitting of H_2O and CO_2. *Energy Fuels.* 2015;29(5):3241–3250.

19. Bonk A, Maier AC, Schlupp MVF, Burnat D, Remhof A, Dermelle R, Steinfeld A, Vogt UF. The effect of dopants on the redox performance, microstructure and phase formation of ceria. *J Power Sources*. 2015; 300:261–271.

20. Scheffe JR, Steinfeld A. Oxygen exchange materials for solar thermochemical splitting of H_2O and CO_2: a review. *Materials Today*. 2014;17(7):341–348.

21. Scheffe JR, Jacot R, Patzke GR, Steinfeld A. Synthesis, characterization, and thermochemical redox performance of Hf^{4+}, Zr^{4+}, and Sc^{3+} doped ceria for splitting CO_2. *J Phys Chem C*. 2013;117(46):24104–24114.

22. Abanades S, Legal A, Cordier A, Peraudeau G, Flamant G, Julbe A. Investigation of reactive cerium-based oxides for H_2 production by thermochemical two-step water-splitting. *J Mater Sci*. 2010;45(15):4163–4173.

23. Kuhn M, Bishop SR, Rupp JLM, Tuller HL. Structural characterization and oxygen nonstoichiometry of ceria-zirconia ($Ce_{1-x}Zr_xO_{2-\delta}$) solid solutions. *Acta Materialia*. 2013;61(11):4277–4288.

24. Call F, Roeb M, Schmücker M, Bru H, Curulla-Ferre D, Sattler C, Pitz-Pall R. Thermogravimetric analysis of zirconia-doped ceria for thermochemical production of solar fuel. *Am J Anal Chem*. 2013;4:37.

25. Hao Y, Yang C-K, Haile SM. Ceria–zirconia solid solutions ($Ce_{1-x}Zr_xO_{2-\delta}$, $x \leq 0.2$) for solar thermochemical water splitting: a thermodynamic study. *Chem Mater*. 2014;26(20):6073–6082.

26. Bulfin B, Call F, Vieten J, Roeb M, Sattler C, Shvets IV. Oxidation and reduction reaction kinetics of mixed cerium zirconium oxides. *J Phys Chem C*. 2016;120(4):2027–2035.

27. Meng Q-L, Lee C-I, Ishihara T, Kaneko H, Tamaura Y. Reactivity of CeO_2-based ceramics for solar hydrogen production via a two-step water-splitting cycle with concentrated solar energy. *Int J Hydrogen Energy*. 2011;36(21):13435–13441.

28. Schunk LO, Steinfeld A. Kinetics of the thermal dissociation of ZnO exposed to concentrated solar irradiation using a solar-driven thermogravimeter in the 1800–2100 K range. *AIChE J*. 2009;55(6): 1497–1504.

29. Levêque G, Abanades S. Design and operation of a solar-driven thermogravimeter for high temperature kinetic analysis of solid–gas thermochemical reactions in controlled atmosphere. *Solar Energy*. 2014; 105:225–235.

30. Schwartzwalder K, Somers AV. Inventors; U.S. Patent 3090094, assignee. Method of making porous ceramic articles. US patent U.S. Patent 30900941963.

31. Vogt UF, Gorbar M, Dimopoulos-Eggenschwiler P, Broenstrup A, Wagner G, Colombo P. Improving the properties of ceramic foams by a vacuum infiltration process. *J Eur Ceramic Soc*. 2010;30(15): 3005–3011.

32. Petrasch J, Coray P, Meier A, Brack M, Häberling P, Wuillemin D, Steinfeld A. A novel 50kW 11,000 suns high-flux solar simulator based on an array of xenon arc lamps. *J Sol Energy Eng*. 2006; 129(4):405–411.